RSC Advances

PAPER

View Article Online
View Journal | View Issue

Cite this: *RSC Adv.*, 2026, **16**, 9547

Electrochemical resolution of purine metabolite overlap using a synthesis-assisted Fe_2O_3-RGO heterointerface

Nguyen Minh Quang,[a] Do Mai Nguyen,[b] Vo Chau Ngoc Anh,[c] Tran Thanh Tam Toan*[d] and Anh-Quang Dao*[ef]

Received 6th December 2025
Accepted 6th February 2026

DOI: 10.1039/d5ra09441k

rsc.li/rsc-advances

An advanced electrochemical sensor was successfully fabricated by modifying a glassy carbon electrode (GCE) with a composite of Fe_2O_3 nanoparticles and reduced graphene oxide (RGO). The resulting Fe_2O_3-RGO/GCE was characterized, and its performance was evaluated for the simultaneous determination of uric acid (UA), xanthine (XA), and hypoxanthine (HX). The oxidation peaks of UA, XA, and HX were clearly separated at approximately +0.3 V, +0.7 V, and +1.2 V, respectively. This remarkable separation, attributed to a synergistic effect between the highly conductive RGO and the catalytic Fe_2O_3, overcomes a significant analytical challenge presented by the overlapping signals of these coexisting purine metabolites. The sensor exhibited a low detection limit of 0.003 μM for UA within a linear range of 0.01 μM to 1.99 μM. Furthermore, the electrode's selectivity was confirmed; common biological interferents, such as ascorbic acid, dopamine, glucose, and urea, did not cause significant signal interference. The method's practical utility was confirmed through the analysis of real urine samples, with results showing high recovery rates and statistical agreement with the standard HPLC method. Additionally, this work provides a sustainable and scalable solution to the persistent challenge of purine metabolite overlap, offering a robust platform for the rapid, low-cost, and decentralised monitoring of metabolic disorders in clinical settings.

1. Introduction

Uric acid (UA), the terminal product of human purine catabolism, has been implicated in gout, nephrolithiasis, and renal-cardiometabolic disorders; its production from hypoxanthine (HX) and xanthine (XA) proceeds *via* two sequential oxidations catalyzed by XA oxidoreductase. In physiological specimens, UA therefore coexists with both precursors, and fluctuations across the triad encode pathway activity and therapeutic response. Under normal physiological conditions, the concentration of uric acid in human serum is maintained within the range of 210 μM to 420 μM for males and 150 μM to 350 μM for females. In urine, the excretion levels typically range from 1.5 mM to 4.4 mM per 24 hours. Deviations from these homeostatic levels are frequently utilized as primary biomarkers for the diagnosis of metabolic disorders.[1] Abnormal elevations in serum uric acid, known as hyperuricemia, are directly implicated in the precipitation of monosodium urate crystals, which leads to gouty arthritis and nephrolithiasis. Furthermore, chronic hyperuricemia is increasingly recognized as an independent risk factor for hypertension, cardiovascular disease, and chronic kidney disease, necessitating precise monitoring tools.[2] This biochemical setting has been clarified by recent accounts of purine metabolism and analytical uses of purine catabolites, underscoring the continued requirement for selective, interference-resistant UA measurements in clinically relevant fluids.[3,4] Conversely, the precursors xanthine and hypoxanthine are present at significantly lower concentrations in healthy human serum, typically ranging from 0.05 μM to 3.0 μM for xanthine and 0.5 μM to 5.0 μM for hypoxanthine. Elevated levels of these metabolites are associated with pathological conditions such as hereditary xanthinuria, resulting from xanthine oxidoreductase deficiency, or Lesch–Nyhan syndrome, a disorder of purine salvage.[5,6]

Currently, the determination of purine metabolites is predominantly performed using high-performance liquid chromatography (HPLC) or enzymatic colorimetric assays. While these methods offer high specificity and accuracy, their widespread application in point-of-care testing is often limited by high operational costs, the requirement for bulky

---

[a] Faculty of Chemical Engineering, Industrial University of Ho Chi Minh City, Ho Chi Minh City, 700000, Vietnam
[b] University of Sciences, Hue University, Hue City, 530000, Vietnam
[c] University of Medicine and Pharmacy, Hue University, 530000, Vietnam
[d] Phu Xuan University, Hue city, 530000, Vietnam. E-mail: tranthanhtamtoan@gmail.com
[e] Faculty of Environmental and Natural Sciences, Duy Tan University, Da Nang, 550000, Vietnam. E-mail: daoanhquang@duytan.edu.vn
[f] Institute of Research and Development, Duy Tan University, Da Nang, 550000, Vietnam

instrumentation, and complex sample pretreatment protocols. They are generally restricted to offline analysis rather than real-time detection due to the necessary sample transport and separation lag times. Consequently, alternative methodologies that offer rapid response times and portability are highly sought after.[5,7] Electrochemical sensing has been adopted as a practical route to UA analysis because rapid readouts can be achieved with low sample volumes and compact instrumentation.[8] Within this domain, differential-pulse voltammetry (DPV) has been favored for trace analytes since non-faradaic contributions are intrinsically minimized and peak resolution is enhanced, allowing closely spaced oxidation processes to be distinguished in complex backgrounds. Recent method papers and reviews have consolidated these advantages, including the pH-dependent shifts in UA peak potentials that reflect proton-coupled oxidation.[1,9,10]

Despite these strengths, a core selectivity bottleneck has persisted at conventional carbon electrodes. The anodic oxidations of HX, XA, and UA occur at proximate potentials and follow related two-electron pathways, so partial peak overlap and mutual signal distortion are frequently observed. Foundational voltammetric studies documented the sequence HX, XA, UA, and the narrow potential spacing across wide pH ranges, explaining why bare electrodes often underperform for multi-analyte purine analysis.[11] To mitigate this limitation, interfacial engineering has been pursued. Polymer films and graphene-based hybrids have yielded improved separations, as illustrated by poly(L-arginine)/graphene films for the UA–XA–HX triad, ferrite/graphene composites that permit simultaneous tri-purine readouts, and newer oxide–carbon platforms tuned for selected purine pairs in urine.[12–15]

Recent advancements in 2024 and 2025 have further underscored the efficacy of heterointerfaces. Reduced graphene oxide (RGO) has served as a conductive, high-area scaffold that accelerates interfacial electron transfer while enriching aromatic analytes through π–π and electrostatic interactions.[16,17] Electrochemical RGO generation is a reagent-free, *in situ* route. For instance, Ramesh (2024) successfully developed N-doped $ZnWO_4$ nanorods decorated on N-doped RGO sheets for the sensitive detection of diphenylamine with a LOD of 0.0083 μM, while Rajaram (2025) reported the hydrothermal synthesis of pure-phase doughnut-like $NiNb_2O_6$ nanostructures on RGO for azathioprine sensing, achieving a LOD of 0.0035 μM. These studies highlight the crucial role of synergistic interactions in enhancing electrochemical performance for environmental and food safety monitoring.[18,19] This method avoids hazardous reductants, allows precise control over oxygen functionality/defect density, and yields films directly on the current collector with low charge-transfer resistance. These features have been detailed in recent reviews and process studies, and have motivated the increasing use of ERGO in sensing architectures, including screen-printed and miniaturized formats.[20–22]

Transition-metal oxides complement graphene by introducing redox-active catalytic sites. Among various candidates, iron(III) oxide (Fe_2O_3) is recognised as an abundant, non-toxic d-block transition-metal oxide. While certain lanthanide-series oxides (*e.g.*, CeO_2 or La_2O_3) have been explored in electrochemical architectures for their unique electronic properties and oxygen storage capacity, d-block oxides remain the preferred candidates for purine analysis owing to their robust catalytic activity and practical scalability. Conversely, the implementation of actinide-series elements is generally precluded in biosensing frameworks due to inherent radiological risks and associated safety protocols.[23–26] Therefore, when iron(III) oxide (Fe_2O_3) is interfaced with RGO, cooperative behaviour is typically observed: RGO furnishes fast electron pathways and adsorption domains, whereas Fe_2O_3 contributes surface hydroxyls and Fe(III)/Fe(II) couples that lower overpotentials and amplify faradaic responses.[27,28] The integration of RGO with Fe_2O_3 is predicated on a synergistic design principle: the RGO nanosheets provide a highly conductive, high-surface-area scaffold that minimises diffusion resistance, while the Fe_2O_3 nanoparticles introduce specific catalytic sites. It is expected that this composite will lower the activation energy for purine oxidation and enhance the adsorption capacity for the analytes, thereby resolving the overlapping signals.[18,19] Recent reports have described Fe_2O_3/graphene hybrids for UA with co-analytes and morphology-dependent activity, and have extended the concept to α-Fe_2O_3/RGO systems engineered for non-enzymatic UA sensing.[27–29]

Within the broader landscape of purine electroanalysis, numerous platforms have demonstrated simultaneous or pairwise detection—ranging from polymer–graphene films and ferrite/rGO composites for the UA–XA–HX triad to oxide-quantum-dot hybrids for UA–HX or UA–XA in urine. Nevertheless, selective UA readout under a persistent HX/XA background has not been systematically established using Fe_2O_3 anchored on ERGO films fabricated entirely by electrochemical potential scanning, despite the sustainability and reproducibility advantages of this green route. The most recent literature has continued to emphasize simultaneous quantification and matrix tolerance, yet explicit demonstration that UA calibration in DPV remains unbiased by its precursors—particularly in complex matrices—has remained comparatively rare.[14,15,30]

In the present work, that interference problem has been addressed directly by constructing a Fe_2O_3-RGO heterointerface on GCE through reductant-free electrochemical RGO, followed by Fe_2O_3 assembly, and by interrogating UA responses with DPV while XA and HX were maintained at fixed, clinically relevant concentrations. The sensing concept has relied on adsorption-controlled preconcentration on ERGO together with Fe_2O_3-mediated catalytic acceleration to widen interpeak separations and to decouple UA kinetics from those of its precursors. Under these conditions, UA calibration slopes and intercepts were shown to be preserved relative to single-analyte conditions, with nanomolar-level detection and agreement with an HPLC reference in urine, establishing that UA can be quantified without bias in the co-presence of XA and HX. With a LOD of 0.003 μM and proven selectivity in urine samples, this platform provides a sustainable, scalable foundation for future point-of-care devices capable of comprehensive purine profiling. The platform thus provides a sustainable, scalable foundation for forthcoming true concurrent UA–XA–HX electroanalysis in complex matrices.

2. Experimental

2.1. Chemicals

The chemicals used in the study, including uric acid (UA), xanthine (XA), hypoxanthine (HX), graphene oxide (GO), graphite, iron(III) oxide (Fe_2O_3), ascorbic acid, urea, dopamine, glucose, calcium nitrate ($Ca(NO_3)_2$), sodium chloride (NaCl), ammonium sulfate ($(NH_4)_2SO_4$), and iron chloride ($FeCl_3$), were all of high purity ≥99%. These chemicals were sourced from Merck, Germany, ensuring the precision and reliability of the electrochemical analysis and the robustness of the sensor.

2.2. Instruments

For the physical and elemental characterization of the material, high-resolution transmission electron microscopy (TEM) was conducted on a Jeol JEM2100 instrument. Morphological and elemental composition were determined using energy-dispersive X-ray spectroscopy (EDX) and scanning electron microscopy (SEM) with a Horiba EMAX ENERGY EX-400 analyzer.

All electrochemical experiments, including cyclic voltammetry and differential pulse voltammetry, were performed using a Corrtest CS350M electrochemical workstation. A standard three-electrode configuration was employed for all electrochemical investigations.

2.3. Preparation of Fe_2O_3-RGO/GCE

2.3.1. Synthesis of GO. Graphene oxide (GO) was prepared using the modified Hummers process.[31] The following process outline describes the synthesis of graphene oxide (GO) from graphite using a series of carefully controlled reactions. Initially, a mixture of sulfuric acid (H_2SO_4) and phosphoric acid (H_3PO_4) in a volume ratio of 360 : 40 (mL mL^{-1}) was prepared and stirred at 30 °C. To this acidic mixture, 18 g of potassium permanganate ($KMnO_4$) was added, followed by 3.0 g of graphite (G), and the resulting solution was allowed to react for 72 hours at 30 °C. Subsequently, 17 mL of 30% hydrogen peroxide (H_2O_2) was added to the solution, which was then transferred into a centrifuge tube for further processing.

The mixture was centrifuged at 6000 rpm for 60 minutes at 30 °C, during which the solid-phase material, characterized by a yellowish-brown color, was formed. The solid was then washed with hydrochloric acid (HCl) solution at a concentration of 1.0 M to remove sulfate ions (SO_4^{2-}) by precipitation with barium chloride ($BaCl_2$). This was followed by washing with distilled water until chloride ions (Cl^-) were completely removed, confirmed by the addition of silver nitrate ($AgNO_3$).

The resulting product was then centrifuged again at 6000 rpm for 60 minutes at 30 °C, and the solid was dried under controlled conditions at 60 °C for 48 hours. The final product obtained from this synthesis was graphene oxide (GO), also referred to as the oxidized graphite product.

2.3.2. Synthesis of Fe_2O_3-GO. Subsequently, iron precursors such as iron(II) sulfate heptahydrate ($FeSO_4 \cdot 7H_2O$) and sodium acetate (CH_3COONa) stabilizing agents were added to the solution. The mixture was stirred vigorously at room temperature for an extended period, allowing for complete interaction between the carbon and iron species. The resulting product was then washed multiple times with deionized (DI) water and ethanol to eliminate any remaining impurities. Afterward, it was dried under controlled conditions, producing the desired Fe_2O_3-GO composite material.[32] This composite, with its unique structural properties, was subsequently utilized for further electrochemical applications.

2.3.3. The preparation of Fe_2O_3-GO/GCE. The GCE electrode was polished carefully using alumina powder (0.05 μm). Afterward, the electrode was thoroughly washed with distilled water two times. The surface of the electrode was further cleaned by sonication in a mixture of ethanol (96%): water (50 : 50, v/v). The GCE electrode was then dried under a heating source at 40 °C. Prior to modification with the composite material, 1 mL of Fe_2O_3-GO (1 mg mL^{-1}) solution was prepared and added onto the electrode surface. Next, 10 μL of 5% Nafion in ethanol (96%) was applied onto the surface to act as a binder and stabilize the composite layer between the Fe_2O_3-GO material and the GCE surface. This was followed by ultrasonic treatment for 10 minutes. Subsequently, 5.0 μL of the composite mixture was dropped onto the GCE surface ($d = 2.8 \pm 0.1$ mm), which was then cleaned and dried under a heating source at 40 °C.

The modified electrode was immersed in a 10.0 mL BRBS buffer solution (pH = 7.0, $C_{\mathrm{BRBS}} = 0.2$ M) to ensure the electrode's surface remained stable for electrochemical measurements. The cyclic voltammetry electrochemical measurements were conducted under ambient aerobic conditions in a solution with an applied potential range from 0 V to −1.5 V *vs.* Ag/AgCl/KCl 3 M for 120 s. The electrode created through this procedure was designated as Fe_2O_3-RGO/GCE.

2.4. Preparation of real samples

Urine samples were collected post-mortem from slaughterhouses in Hue City, Central Vietnam. These mammalian samples were specifically selected to serve as a representative complex biological matrix, sharing key compositional characteristics (*e.g.*, high ionic strength, urea, and protein content) with human urine. This choice enables a rigorous evaluation of the sensor's analytical performance and robustness in a realistic physiological environment, without the immediate need for human volunteers at this developmental stage. To prepare the non-spiked (blank) sample, 1 mL of urine was mixed with 2 mL of BRBS buffer, and deionized (DI) water was added to adjust the total volume to 10 mL. The mixture was then centrifuged and filtered through a membrane with a pore size of 0.46 μm.

For the spiked samples, 1 mL of urine was spiked with UA at a concentration of 20 μM, mixed with 2 mL of BRBS buffer, and DI water was added to achieve a final volume of 10 mL. The resulting solution contained 20 μM of uric acid. The sample was then centrifuged and filtered using the same membrane filter as for the non-spiked sample.

Both non-spiked and spiked solutions were analyzed for uric acid content using the DPV method developed in this study.

3. Results and discussions

3.1. Characterizations of Fe_2O_3-RGO

In Fig. 1a, a continuous graphene sheet was observed with clear wrinkles and folded edges. The surface appeared free of bright particulates, which indicated that oxide domains had not yet formed and that defect and edge sites on reduced graphene remained available for later nucleation. In Fig. 1b, iron oxide appeared as discrete bright particles with narrow size dispersion and sharp boundaries when viewed without a carbon host. Their local contacts suggested a phase with high surface energy that tends to approach one another in the absence of a supporting sheet. In the SEM image of the composite (Fig. 1c), the individual components are distinguishable by their morphological and contrast differences. The Fe_2O_3 nanoparticles are identified as the bright, granular features that are uniformly distributed across the surface. These particles are anchored onto the underlying RGO support, which is visible as the darker, wrinkled sheets providing a continuous conductive network. This distinction is further resolved in the TEM analysis (Fig. 1d). Here, the high-density Fe_2O_3 clusters appear as dark, opaque aggregates (due to mass-thickness contrast) dispersed on the lighter, semi-transparent background of the RGO nanosheets. This clear contrast boundary confirms that the metal oxide is physically immobilized on the carbon scaffold rather than being a physical mixture. Direct contact between particle edges and the carbon surface was evident. Although nanoparticles have a natural tendency to aggregate, the RGO sheets effectively acted as a support matrix, minimising severe agglomeration and ensuring that the Fe_2O_3 active sites remained accessible to the electrolyte.

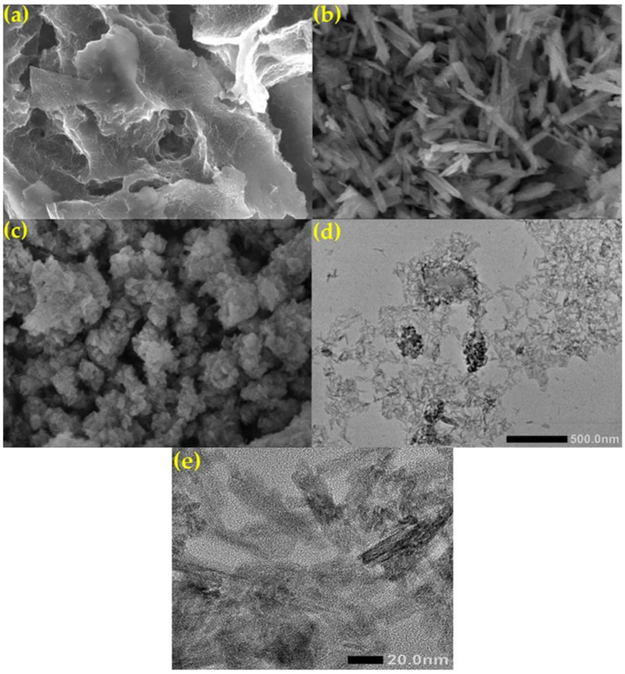

Fig. 1 (a–c) The SEM images of RGO, Fe_2O_3, and Fe_2O_3-RGO, (d and e) HRTEM image of Fe_2O_3-RGO.

As shown in Fig. 1e, the lattice fringes of the anchored nanoparticles are explicitly resolved. The measured interplanar spacing corresponds precisely to the lattice parameters of the hematite phase (Fe_2O_3). This direct lattice imaging confirms that the synthesis conditions favored the formation of a highly crystalline iron oxide phase anchored on the carbon scaffold. This intimate contact between the crystalline oxide and the carbon scaffold, visualized clearly in the fringe patterns, underpins the synergistic heterointerface. The five figures build a coherent progression from a receptive carbon scaffold to a finely divided oxide phase, and finally to a uniform composite with crystalline iron oxide anchored on conductive graphene. This sequence provides the structural basis required later for fast electron transfer and the formation of abundant catalytic sites on the modified glassy carbon electrode.[27,33,34]

The electron images provided a composition-sensitive view that complemented Fig. 1. Regions rich in iron appeared bright, and the graphene matrix appeared darker, which is the expected contrast from electrons that are backscattered more strongly from elements of larger mean atomic number. In Fig. 2a, the field was dominated by the bright oxide. In Fig. 2b, the bright features were spread across the darker carbon sheets and followed the sheet topography. This confirmed that the oxide phase was broadly anchored on the graphene network and not segregated into isolated clusters. The contrast pattern, therefore, supported the interfacial picture established in Fig. 1c and d.[34,35]

The structural properties of the synthesized materials were further investigated using X-ray diffraction (XRD) and Raman spectroscopy. Fig. 3a presents the XRD patterns of graphite, GO, RGO, Fe_2O_3, and the Fe_2O_3-RGO composite. The graphite spectrum exhibits a sharp characteristic peak at $2\theta = 26.5°$, corresponding to the (002) plane. Upon oxidation to GO, this peak disappears and is replaced by a new peak at 10.6°. Following the reduction process, the RGO spectrum exhibits a broad diffraction peak centered at 24.5°, indicating the removal of functional groups and partial restoration of the graphitic structure. The XRD pattern of the pure Fe_2O_3 nanoparticles displays distinct diffraction peaks that are well-indexed to the rhombohedral phase of hematite (α-Fe_2O_3) (JCPDS No. 33-0664).[36,37] In the spectrum of the Fe_2O_3-RGO composite, all the characteristic peaks of hematite are clearly observed. Nevertheless, the typical broad peak of RGO is not distinctly visible, likely due to the high crystallinity of the iron oxide nanoparticles, which may overshadow the weaker carbon signal, or because the RGO sheets are effectively prevented from restacking by the anchored nanoparticles. These diffraction results confirm the successful formation of the composite material with high phase purity.[36,37]

Fig. 3b displays the Raman spectra, which provide insights into the defect density and structural order of the carbon materials. The spectra for GO, RGO, and the composite all exhibit two prominent bands: the D band at approximately

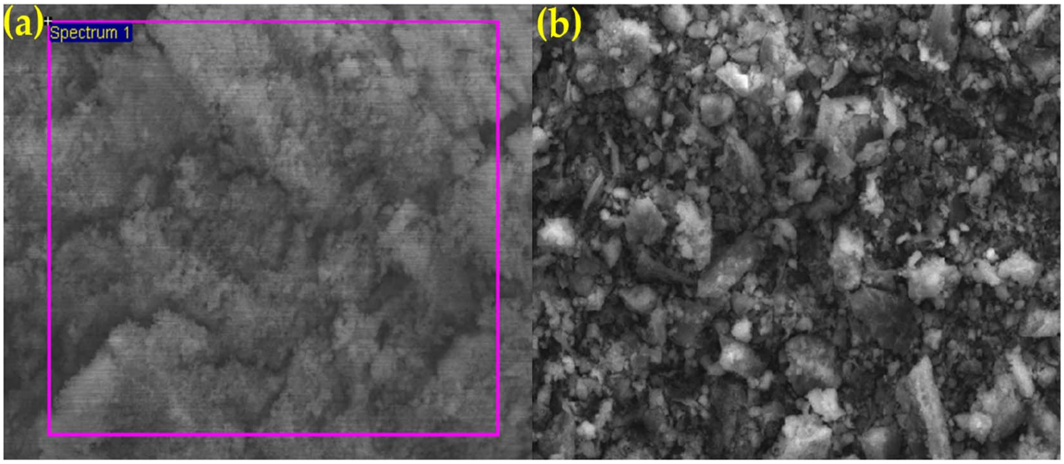

Fig. 2 Electron image of (a) Fe_2O_3 and (b) Fe_2O_3-RGO.

1350 cm^{-1}, associated with structural defects and disordered carbon, and the G band at around 1580 cm^{-1}, related to the in-plane vibration of sp^2-bonded carbon atoms. The intensity ratio of the D band to the G band (I_D/I_G) serves as a key indicator of the degree of disorder. The I_D/I_G ratio was calculated to be 0.92 for GO and increased to 1.15 for RGO. This increase suggests a reduction in the average size of the sp^2 domains upon reduction and the creation of new graphitic domains that are smaller in size but more numerous, a phenomenon commonly observed during the chemical or thermal reduction of GO. For the Fe_2O_3-RGO composite, the presence of characteristic iron oxide bands in the low-frequency region (200–600 cm^{-1}) further confirms the incorporation of Fe_2O_3. The slight shift in the G band position in the composite compared to pure RGO suggests

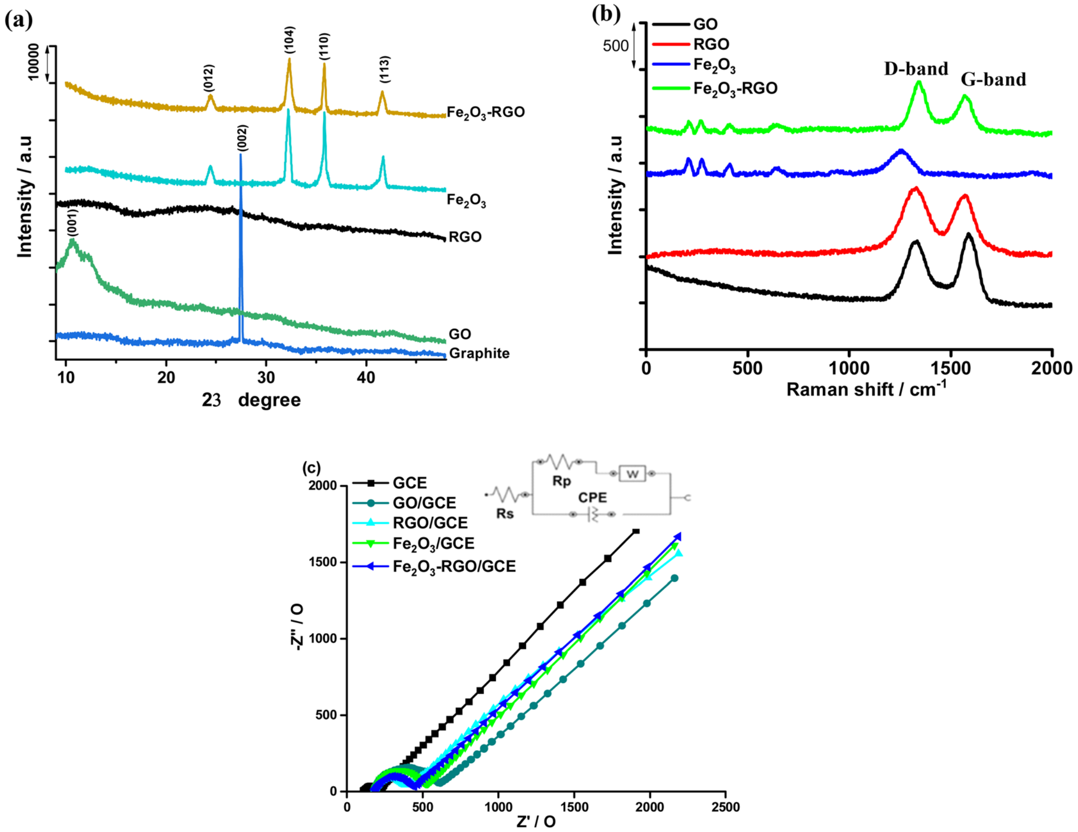

Fig. 3 (a) XRD spectra of graphite, graphene oxide (GO), reduced graphene oxide (RGO), Fe_2O_3 and Fe_2O_3-RGO; (b) Raman spectra of GO, RGO, Fe_2O_3 and Fe_2O_3-RGO; (c) Nyquist plots recorded from electrochemical impedance spectroscopy of 0.5 mM $[Fe(CN)_6]^{3-}/^{4-}$ at a frequency from 100 to 10 MHz recorded on bare GCE, RGO/GCE, Fe_2O_3/GCE and Fe_2O_3-RGO/GCE in 0.2 M BRBS buffer solution. (The inset presents the equivalent circuit model of the electrode/electrolytes).

a charge transfer interaction between the graphene sheets and the metal oxide nanoparticles. These spectral features are consistent with recent reports on graphene-metal oxide hybrids.[18,19]

The electrochemical properties of the modified electrodes were evaluated using electrochemical impedance spectroscopy (EIS). Fig. 3c shows the Nyquist plots for the bare GCE, Fe_2O_3/GCE, RGO/GCE, and Fe_2O_3-RGO/GCE in a solution containing 0.5 mM $[Fe(CN)_6]^{3-}/^{4-}$ as a redox probe. The plots generally consist of a semicircle in the high-frequency region, representing the charge transfer resistance (R_{ct}), and a linear part in the low-frequency region, corresponding to the diffusion process. The data were fitted to a Randles equivalent circuit (inset of Fig. 3c). The bare GCE exhibited a relatively small semicircle with an R_{ct} value of approximately 90 Ω. Upon modification with GO, the resistance increased significantly to 341 Ω due to the insulating nature of the oxygenated functional groups. After reduction, the RGO/GCE showed a decrease in R_{ct} to 202 Ω, reflecting the restoration of electrical conductivity. The Fe_2O_3/GCE displayed a higher resistance of 307 Ω compared to the bare GCE, likely due to the semiconducting nature of the oxide. Most notably, the Fe_2O_3-RGO/GCE composite electrode exhibited a reduced R_{ct} value of 253 Ω relative to the Fe_2O_3/GCE. This improvement indicates that the conductive RGO network effectively facilitates electron transfer between the electrolyte and the electrode surface, mitigating the resistance of the iron oxide particles. This trend in impedance behavior supports the conclusion that the composite material exhibits superior electrochemical characteristics, making it suitable for sensing applications.[27,28]

The spectra from EDX analysis supplied the elemental fingerprints that underpinned the images. Fig. 4a of Fe_2O_3 showed the expected lines of iron and oxygen. Fig. 4b of the composite showed iron and oxygen, along with a strong carbon signal from the graphene scaffold, and no peaks of foreign species at significant intensity. The close match between the intended iron oxygen carbon composition and the measured spectra supported a clean interface between oxide and carbon, and agreed with the composite morphology demonstrated by the electron images.[27,36,38]

The quantitative EDX results provided a numerical representation of the structural picture (Table 1). For Fe_2O_3, the measured weights were about sixty-five percent iron and thirty-five percent oxygen, which is compatible with hematite within the known tolerance of the method. After incorporation of RGO, the composite showed an increase in carbon to about one-third of the total, a lower apparent iron fraction, and a modest change in oxygen, which is consistent with dilution by a light carbon matrix and partial absorption effects in a low atomic number support. These values are therefore consistent with a uniform dispersion of oxide on a continuous carbon framework rather than a physical mixture of separate phases.[36,37]

3.2. Electrochemical detection of UA in the dual presence of XA and HX

3.2.1. The electrode behavior. As shown in Fig. 5a, the bare GCE exhibits a very weak current response and poorly defined peaks for all three analytes. This is a well-documented limitation of conventional electrodes, underscoring the necessity of surface modification. The RGO/GCE shows an improved current response, which can be attributed to the high conductivity and large surface area of the RGO. The improved current response is attributed to the RGO's large electroactive surface area, which is structurally preserved by the material's morphology. As evidenced by the wrinkled texture and nanoparticle spacers seen in Fig. 1, the composite architecture effectively inhibits the restacking of graphene sheets, thereby maintaining a highly porous network that maximizes analyte accessibility and interfacial contact. Nevertheless, the oxidation peaks of the three analytes remain unresolved. Similarly, the Fe_2O_3/GCE shows a slight increase in peak currents compared to the bare GCE, which is likely due to the electrocatalytic effect of the ferric oxide nanoparticles. Cyclic voltammetry of the modified electrode in blank BRBS buffer (pH 7.0) displayed a stable, featureless background current within the potential window,

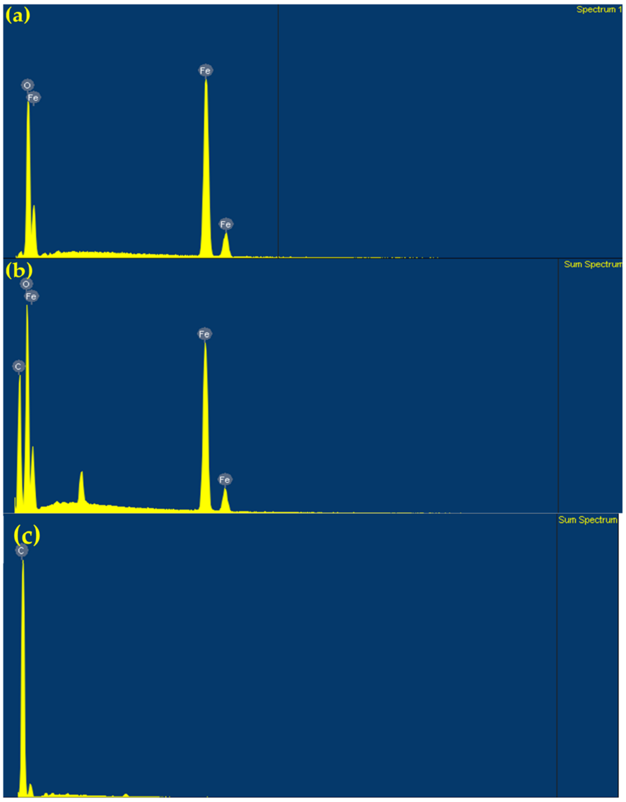

Fig. 4 EDX spectra of (a) Fe_2O_3, (b) Fe_2O_3-RGO and (c) RGO.

Table 1 The element distribution of Fe_2O_3, Fe_2O_3-RGO and RGO

	%Weight (total 100%)		
Materials	Fe	O	C
Fe_2O_3	64.93	35.07	
Fe_2O_3-RGO	27.29	40.05	32.66
RGO			100.0

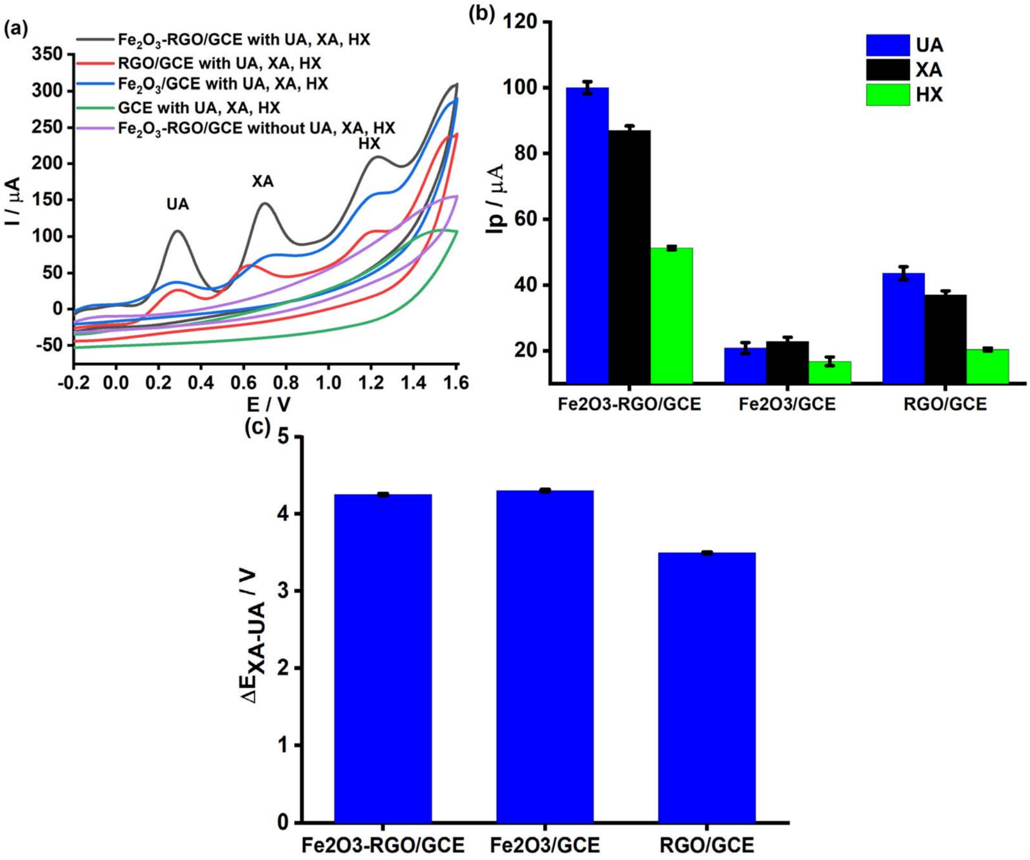

Fig. 5 (a) CVs of 50 μM UA, XA, and HX at various electrodes, (b) peak currents (I_p) for UA, XA, and HX at different electrodes, and (c) ΔE_p values between UA and XA for each electrode.

confirming that the peaks observed in Fig. 5a originate solely from the faradaic oxidation of the analytes.

In contrast, the Fe_2O_3-RGO/GCE exhibits a remarkable enhancement in both peak currents and peak resolution. The peaks for UA, XA, and HX are clearly separated and significantly intensified. The oxidation peak potentials were observed at +0.3 V for UA, +0.7 V for XA, and +1.2 V for HX. This pronounced improvement is a result of the synergistic effect between the highly conductive RGO sheets and the catalytically active Fe_2O_3 nanoparticles. The RGO acts as a high-speed electron transfer pathway, while the Fe_2O_3 nanoparticles provide abundant active sites that lower the overpotential and facilitate the oxidation process for all three analytes.

The bar charts in Fig. 5b and c provide a quantitative validation of the observations from the voltammograms. Fig. 5b confirms that the peak currents for UA, XA, and HX are significantly higher on the Fe_2O_3-RGO/GCE than on the other electrodes. This quantitative evidence supports the claim that the Fe_2O_3-RGO nanocomposite enhances the electrocatalytic activity and electron transfer kinetics at the electrode-solution interface. Furthermore, the data presented in Fig. 5c are particularly compelling. The peak potential separation (ΔE_p) between UA and XA, calculated to be approximately 0.43 V, is shown to be significantly larger at the Fe_2O_3-RGO/GCE compared to the RGO/GCE and Fe_2O_3/GCE. A larger ΔE_p is a direct indicator of enhanced selectivity, as it ensures that the oxidation peaks do not overlap, thereby enabling the reliable simultaneous determination of the analytes.

In conclusion, the results from Fig. 5 collectively demonstrate that the Fe_2O_3-RGO nanocomposite-modified electrode is the most effective among the evaluated electrodes. The combined benefits of high sensitivity (large currents) and excellent selectivity (well-separated peaks) make it a highly promising platform for the simultaneous determination of UA, XA, and HX compared to the other modified electrodes evaluated.

3.2.2. The impact of pH. The influence of pH on the electrochemical response of UA, XA, and HX was a pivotal aspect of the method's optimization. A series of cyclic voltammograms (CVs) was recorded for a solution containing all three analytes across a pH range from 3 to 9, with the findings being illustrated in Fig. 6a. This pH range (3.0–9.0) was selected to cover the physiological pH and the pK_a values of the analytes, allowing for the comprehensive optimization of proton-coupled electron transfer kinetics. A clear dependence of both the oxidation peak current (I_p) and the oxidation peak potential (E_p) on the pH of the supporting electrolyte was consistently observed.

Fig. 6b quantitatively demonstrates the dependence of the peak current (I_p) on the pH of the buffer solution for UA, XA, and

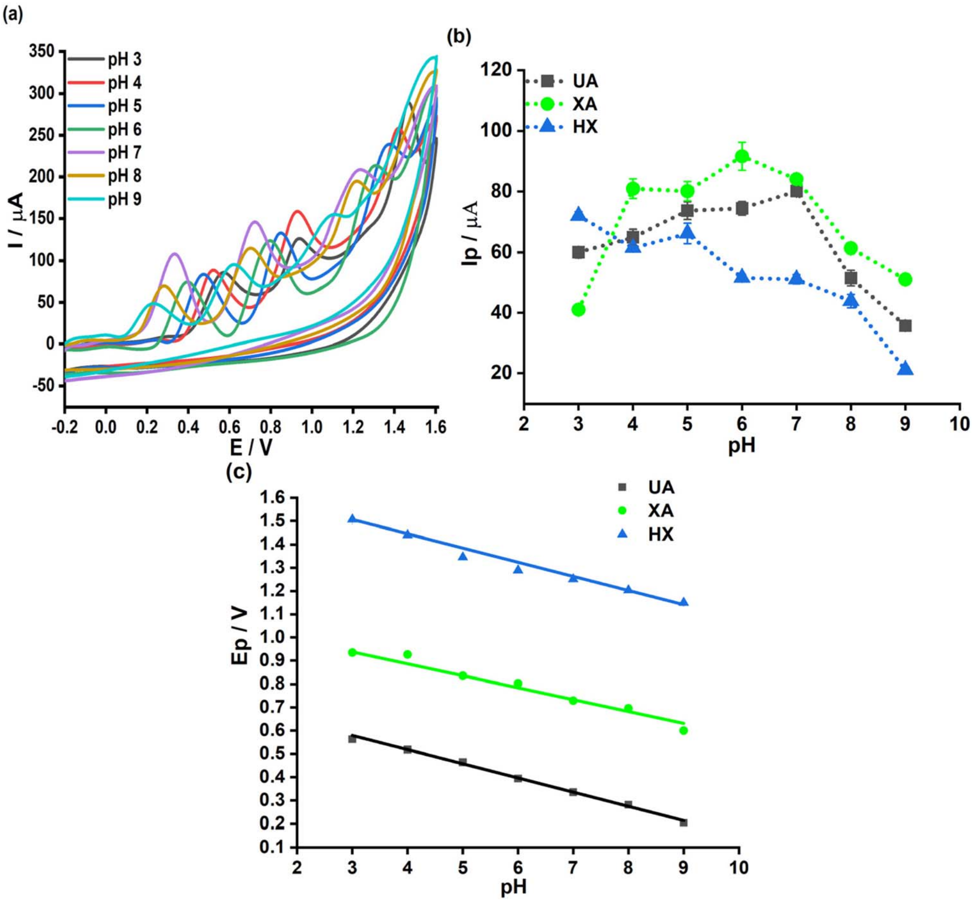

Fig. 6 (a) The CVs of UA, XA, and HX at different pH levels with Fe_2O_3-RGO/GCE, (b) a plot of I_p (μA) *vs.* pH for UA, XA and HX, (c) a plot of E_p (V) *versus* pH for UA, XA and HX.

HX. This plot provides critical information for identifying the most suitable pH conditions for the simultaneous analysis of these three compounds. For UA, the peak current is observed to increase slightly from pH 3 to pH 6, reaching a relatively high and stable value within the pH 6–7 range. However, as the pH continues to increase above 7, the UA signal begins to decrease significantly. This can be attributed to UA's weak acid nature and the proton-coupled nature of its electrochemical oxidation. As the pH increases, the deprotonation of UA becomes more prevalent, which diminishes the rate of the oxidation reaction and results in a lower peak current.

Similarly, for XA and HX, analogous trends are observed. Specifically, the peak current for XA reaches its maximum value at pH 6, while HX exhibits its highest peak current at pH 3. However, the selection of the optimal pH is not solely dependent on maximizing the signal for each individual analyte but must also ensure the best possible separation of the oxidation peaks for the entire mixture. From the voltammograms shown in Fig. 5a, it is evident that at pH 3 and pH 4, the peaks of the three analytes tend to overlap considerably, making accurate quantitative analysis difficult. In contrast, at pH 7, even though the UA peak current is not at its absolute maximum, the oxidation peaks of all three analytes are observed to be sharp, well-defined, and sufficiently separated. Therefore, based on this crucial balance between sensitivity (current intensity) and resolution (peak separation), pH 7 is identified as the most suitable condition for the simultaneous determination of UA, XA, and HX. Choosing this pH not only optimizes the critical signals but also ensures high accuracy in the complex analytical environment where these co-existing metabolites are present.

Further insights into the oxidation process were gained from the plot of peak potential *versus* pH, as shown in Fig. 6c. A linear negative shift in E_p was observed with increasing pH for all three analytes, indicating that protons are directly involved in the rate-determining step of the electrochemical oxidation. The regression equations of E_p with pH are as follows:

$$E_{p,UA}\ (V) = (-0.061 \pm 0.002) \times pH + (0.762 \pm 0.013),\quad R^2 = 0.995 \tag{3.1}$$

$$E_{p,XA}\ (V) = (-0.061 \pm 0.001) \times pH + (1.689 \pm 0.003),\quad R^2 = 0.999 \tag{3.2}$$

$$E_{p,HX}\ (V) = (-0.051 \pm 0.006) \times pH + (1.090 \pm 0.029),\quad R^2 = 0.938 \tag{3.3}$$

Based on the Nernst equation, at $T = 298$ K (25 °C), the relationship between E_p and pH of a pair of conjugated redox would be expressed as follows the formula:[39]

$$E_p = E^0 + \frac{0.059}{n}\log\frac{Ox^a}{R^b} - 0.059\frac{m}{n}\text{pH} \tag{3.4}$$

where m and n correspond to the number of protons and electrons that participate in the electrochemical reaction on the Fe_2O_3-RGO/GCE electrode surface.

The slopes of the E_p *vs.* pH plots were found to be approximately 0.061, 0.061, and 0.051 V for UA, XA, and HX, respectively. These values are in proximity to the theoretical Nernstian slope of 0.059 V at 25 °C, which strongly suggests that the oxidation of each analyte involves an equal number of electrons and protons.

3.2.3. The impact of scan rates. The reaction kinetics occurring at the modified electrode interface were further elucidated by examining the influence of the potential scan rate (ν) on the electrochemical behavior of UA, XA, and HX. As illustrated in Fig. 7a, cyclic voltammograms recorded across a range of scan rates revealed that the anodic peak currents increased proportionally with the scan rate. Concurrently, a distinct positive shift in the oxidation peak potentials (E_p) was observed for all three analytes as the scan rate increased. This shift towards more positive potentials is a characteristic feature of an irreversible electrochemical process, indicating that the electron transfer rate is slower than the mass transport rate at higher scanning speeds.

Fig. 7c gives the data for the linear correlation of I_{pa} and $\nu^{1/2}$:

$$I_{p,\,UA} = (60.8 \pm 11.2)\ln\nu + (165.8 \pm 17.4);\ R^2 = 0.854 \tag{3.5}$$

$$I_{p,\,XA} = (52.6 \pm 3.7)\ln\nu + (180.3 \pm 5.7);\ R^2 = 0.976 \tag{3.6}$$

$$I_{p,\,HX} = (68.3 \pm 5.0)\ln\nu + (206.8 \pm 7.7);\ R^2 = 0.974 \tag{3.7}$$

The adsorption determines the procedure of the electrode surface, as the linear plot of I_p against $\ln\nu$ does not go through the origin.[40,41] According to eqn (3.5)–(3.7), this indicates that the linear correlation between I_p and $\ln\nu$, as well as the regression equation, does not extend to the origin. This information displays that the UA, XA and HX electro-oxidation procedure is affected by adsorption.

To quantitatively evaluate the kinetic parameters governing this irreversible oxidation, the relationship between the peak potential (E_p) and the natural logarithm of the scan rate ($\ln\nu$) was investigated. As depicted in Fig. 7b, a linear correlation was observed for UA, XA, and HX, further confirming the irreversibility of the electrode reaction. The linear regression equations describing the dependence of E_p on $\ln\nu$ for each analyte were derived from the experimental data and are expressed as follows:

$$E_{p,\,UA} = (0.025 \pm 0.002)\ln\nu + (0.378 \pm 0.002);\ R^2 = 0.980 \tag{3.8}$$

$$E_{p,\,XA} = (0.026 \pm 0.002)\ln\nu + (0.774 \pm 0.003);\ R^2 = 0.976 \tag{3.9}$$

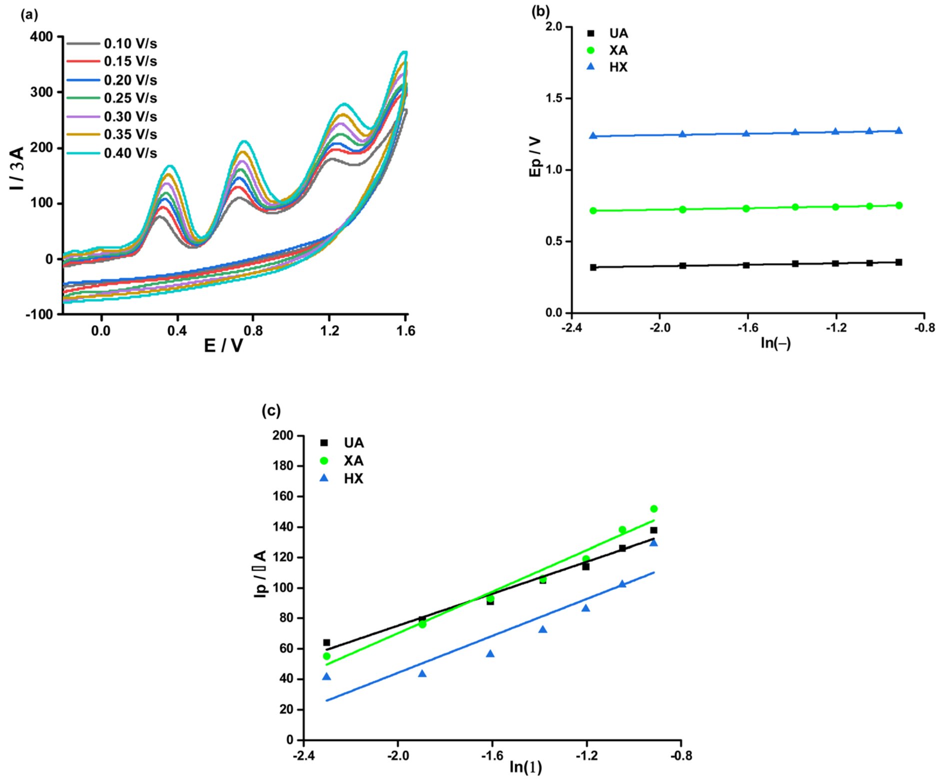

Fig. 7 (a) The CVs of UA, XA, and HX at various scan rates employing Fe_2O_3-RGO/GCE, (b) a plot of E_p (V) *vs.* ln(ν) for UA, XA, and HX and (c) the linear plot of I_p *vs.* lnν for UA, XA and HX.

$$E_{\text{p, HX}} = (0.026 \pm 0.002)\ln \nu + (1.296 \pm 0.002);\ R^2 = 0.982 \quad (3.10)$$

with the Laviron E. assistant.[42] The electrons that are transferred within the reaction of electrochemistry took place on the electrode's surface, might be defined by creating the relation of E_{p} and $\ln \nu$ as follows:

$$E_{\text{pa}} = E^0 - \frac{RT}{(1-\alpha)nF}\ln\frac{RTK_{\text{s}}}{(1-\alpha)nF} + \frac{RT}{(1-\alpha)nF}\ln \nu \quad (3.11)$$

where: $R = 8.314$ J mol^{-1} K, $T = 298$K (25 °C), $F = 96\,500$ C mol^{-1}. With $\alpha = 0.5$, the n value at the anodic peak of UA, XA, and HX is 2.05 (∼2), 1.94 (∼2), and 1.96 (∼2), respectively.[43]

Based on the observed electrochemical behavior and established pathways in the literature[44,45] a tentative oxidation mechanism for UA, XA, and HX is proposed in Scheme 1. While the precise atomistic interactions at the composite interface remain to be fully elucidated, the electrode process is inferred to be driven by a synergistic mechanism where analytes are first pre-concentrated *via* π–π interactions with the RGO basal plane. Subsequently, the Fe-mediated oxidation proceeds according to Scheme 1, involving successive $2e^-/2H^+$ transfers that convert HX to XA, and XA to UA, which is ultimately oxidized to the final product. This mechanism aligns with the Nernstian behavior observed in the pH studies.

3.2.4. The electrochemically active surface area. The cyclic voltammetry (CV) method was used to determine the effective surface area of the electrode by recording the peak current signal of a solution containing 1 mM $K_3[Fe(CN)_6]/K_4[Fe(CN)_6]$ at varying scan rates (Fig. 8a–d). The relationship between the square root of the scan rate and the peak current intensity follows the Randles–Sevcik equation[46] as follows:

$$I_{\text{pa}} = (2.69 \times 10^5)n^{3/2}AD_0{}^{1/2}Cv^{1/2} \quad (3.12)$$

where I_{pa} is peak current (anodic peak current), n is the number of electrons transferred ($n =$ in the $[Fe(CN)_6]^{3-/4-}$ redox system),

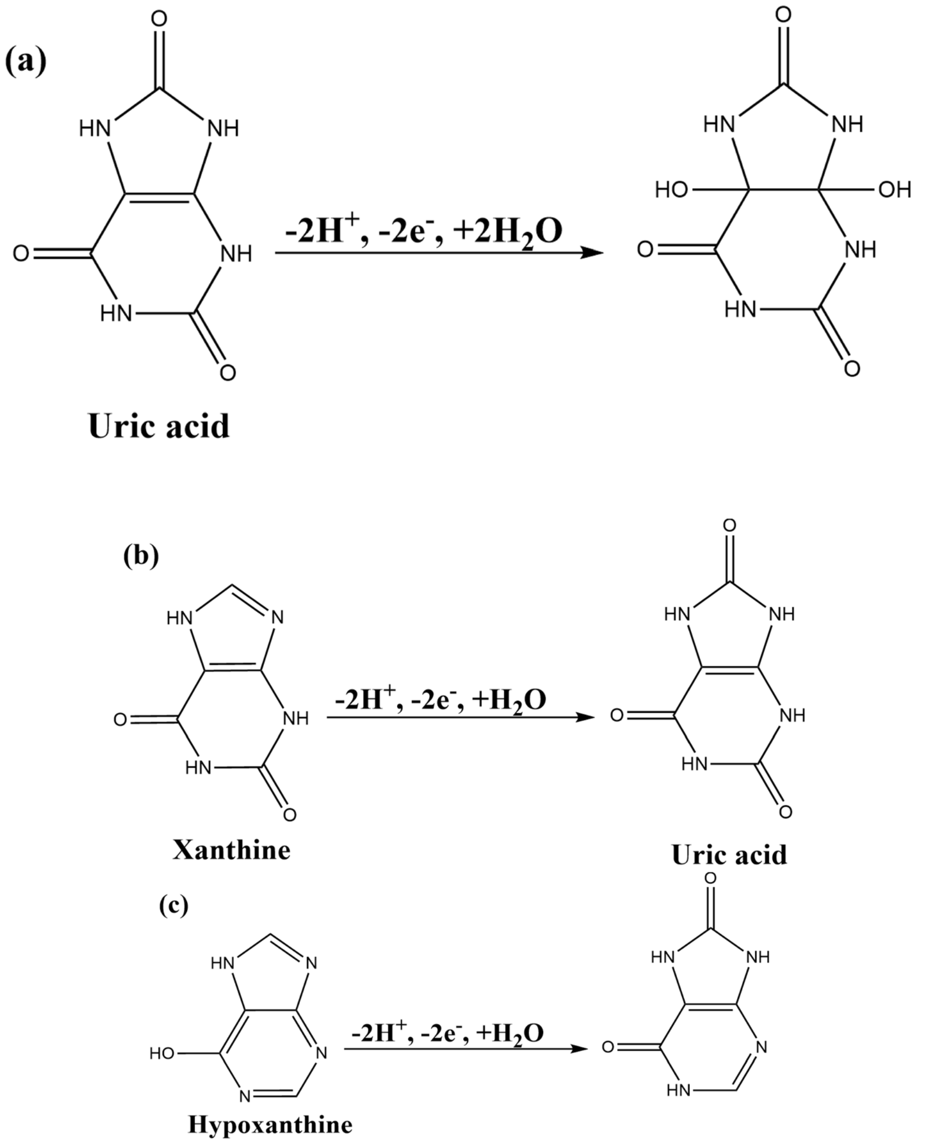

Scheme 1 The proposed mechanism for the (a) UA, (b) XA, and (c) HX oxidation.[30,31]

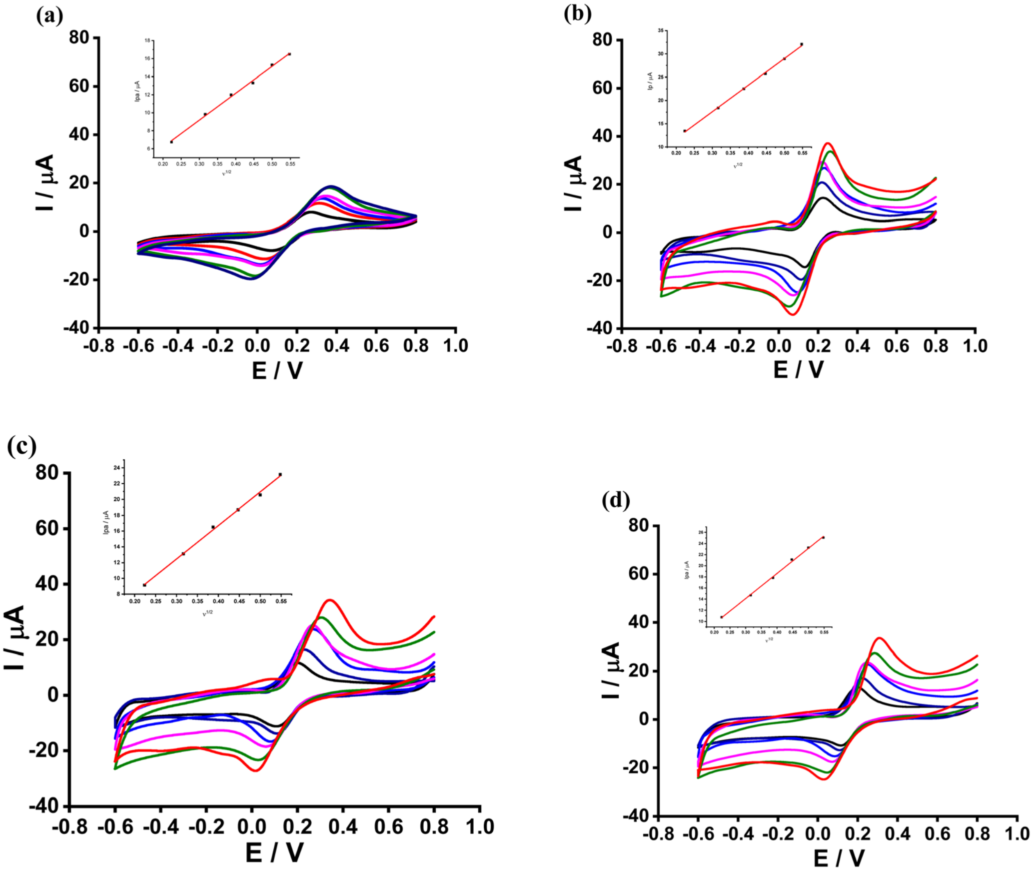

Fig. 8 (a–d) The CVs using bare GCE, Fe_2O_3/GCE, RGO/GCE and Fe_2O_3-RGO/GCE in 1.0 mM $K_3[Fe(CN)_6]/K_4[Fe(CN)_6]$ solution (0.1 M KCl) (inset: the linear plot between $v^{1/2}$ *vs.* I_{pa}).

A is the surface area of electrode (cm^2), *C* is the concentration of $[Fe(CN)_6]^{3-}$, D_0 is the diffusion coefficient of the $[Fe(CN)_6]^{3-/4-}$ (For the $K_3[Fe(CN)_6]/K_4[Fe(CN)_6]$ system, $n = 1$; $C = 1$ mM; $D_0 = 7.6 \times 10^{-6}$ $cm^2 s^{-1}$), and ν is scan rate (V s^{-1}).[46,47]

The values of *A* are found to be 0.040 cm^2 for bare GCE and 0.057, 0.077, and 0.061 cm^2, respectively, for RGO/GCE, Fe_2O_3/GCE, and Fe_2O_3-RGO/GCE. The surface area of Fe_2O_3-RGO/GCE is notably larger than that of the bare GCE, demonstrating the effectiveness of the Fe_2O_3-RGO composite in increasing the electrode's active surface area. This increase in surface area provides more active sites for electrochemical reactions, thereby improving the interaction between the electrode and the analytes.

3.2.5. Linear range and limit of detection.

To comprehensively evaluate the sensor's performance, measurements were conducted under two distinct conditions. This approach aimed to establish both the fundamental sensitivity of the electrode and its capability within a complex environment.

The first case, illustrated in Fig. 9a, involved the determination of UA in a single-analyte solution. DPVs were recorded as the UA concentration was incrementally increased from 0.01 µM to 1.99 µM, revealing a proportional and well-defined enhancement of the peak current at +0.3 V. Crucially, no significant oxidation peaks were observed at the potentials of +0.7 V and +1.2 V (corresponding to XA and HX, respectively), confirming the purity of the single-analyte environment and the absence of interference in this baseline study. This linear relationship was confirmed by the calibration plot in Fig. 9b, which yielded a linear regression equation:

$$I_p\ (\mu A) = (12.07 \pm 0.40) \times C_{UA,\ \mu M} + (0.39 \pm 0.02)\ R^2 = 0.996 \tag{3.13}$$

The limit of detection (LOD) was calculated using the formula $3\sigma/S$, where σ is the standard deviation, and *S* is the slope of the calibration curve. Under these conditions, the LOD for UA was calculated to be 0.004 µM. These results established a robust performance benchmark for the detection of UA in isolation.

The core objective of this research, however, was the ability to analyze UA within a more complex matrix containing its metabolic precursors, XA and HX. To accurately simulate this biological condition, a second set of experiments was performed. In this case, the DPVs were recorded while the UA concentration was increased from 0.01 µM to 1.99 µM, with the concentrations of XA and HX held constant at 1.0 µM. This crucial test was designed to definitively prove that the signal of UA is not compromised by the presence of these structurally similar compounds.

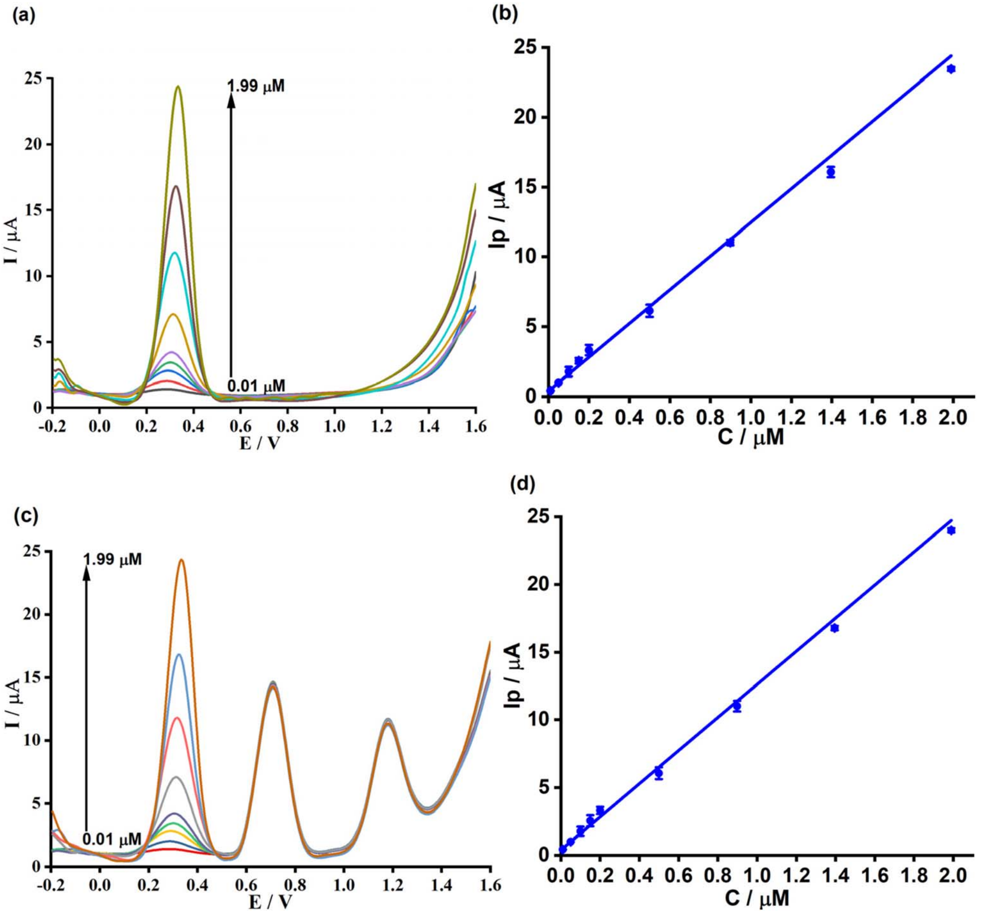

Fig. 9 (a) DPVs of UA in the increasing concentrations: 0.01–1.99 μM, with no existence of XA and HX, (b) linear plot between I_p (μA) for UA and C_{UA} (μM), (c) DPVs of UA in the increasing concentration range: 0.01–1.99 μM, $C_{XA} = C_{HX} = 1.0$ μM, (d) linear relationship of I_p (μA) for UA with C_{UA} (μM).

The results of this pivotal experiment, presented in Fig. 9c, demonstrate that even in the presence of these potential interferents, the UA peak current continued to increase linearly. This linearity was not diminished by the presence of XA and HX. The calibration plot derived from this data (Fig. 9d) produced a linear regression equation

$$I_p\ (\mu A) = (12.24 \pm 0.34) \times C_{UA,\mu M} + (0.38 \pm 0.02) \quad R^2 = 0.997 \tag{3.14}$$

More importantly, the LOD and LOQ were orderly calculated in this case to be 0.003 μM and 0.01 μM, indicating that the sensitivity (12.24 $\mu A\ \mu M^{-1}\ cm^{-2}$) was, in fact, slightly enhanced in the multi-analyte environment. A direct comparison of the two calibration curves reveals a striking similarity in both the slope (sensitivity) and the intercept. This remarkable agreement provides conclusive evidence that the electrochemical signal of UA is independently measured and is not compromised by the presence of XA and HX. This finding represents a significant advancement in the field, validating the exceptional selectivity of the modified electrode and confirming its suitability for the reliable and accurate determination of UA in complex biological samples.

To contextualize the performance of this study, the analytical figures of merit were compared with those of other recently reported electrochemical sensors for the simultaneous determination of UA with other co-existing species. The results, summarized in Table 2. The performance of the proposed Fe_2O_3-RGO electrochemical sensor is highly competitive, achieving a LOD of 0.003 μM for UA. This value is among the

Table 2 Comparison of the analytical performance of the Fe_2O_3-RGO/GCE with other published UA sensors

Materials	Linear range (μM)	LOD (μM)	Ref.
PCL/PEI/MB/Uox/QD	5.0–52	1.85	49
Co-organic framework/CB	0.4–40	0.02	50
Fe_xO_y/UNC	2–20	0.29	51
ZnO–CuO	2–20	0.28	5
Eni-h-MoS_2	10–90	7.3	52
BSAT	20–10	2.1	53
pAR/aPGE	0.09–11	0.03	54
Mn-BDC@MWCNT	0.02–11	0.005	55
N-PCNPs	4–50	0.0002	56
Pt NPs/GDY	0.1–75	0.03	2
Fe_2O_3-RGO	0.01–1.99	0.003	This work

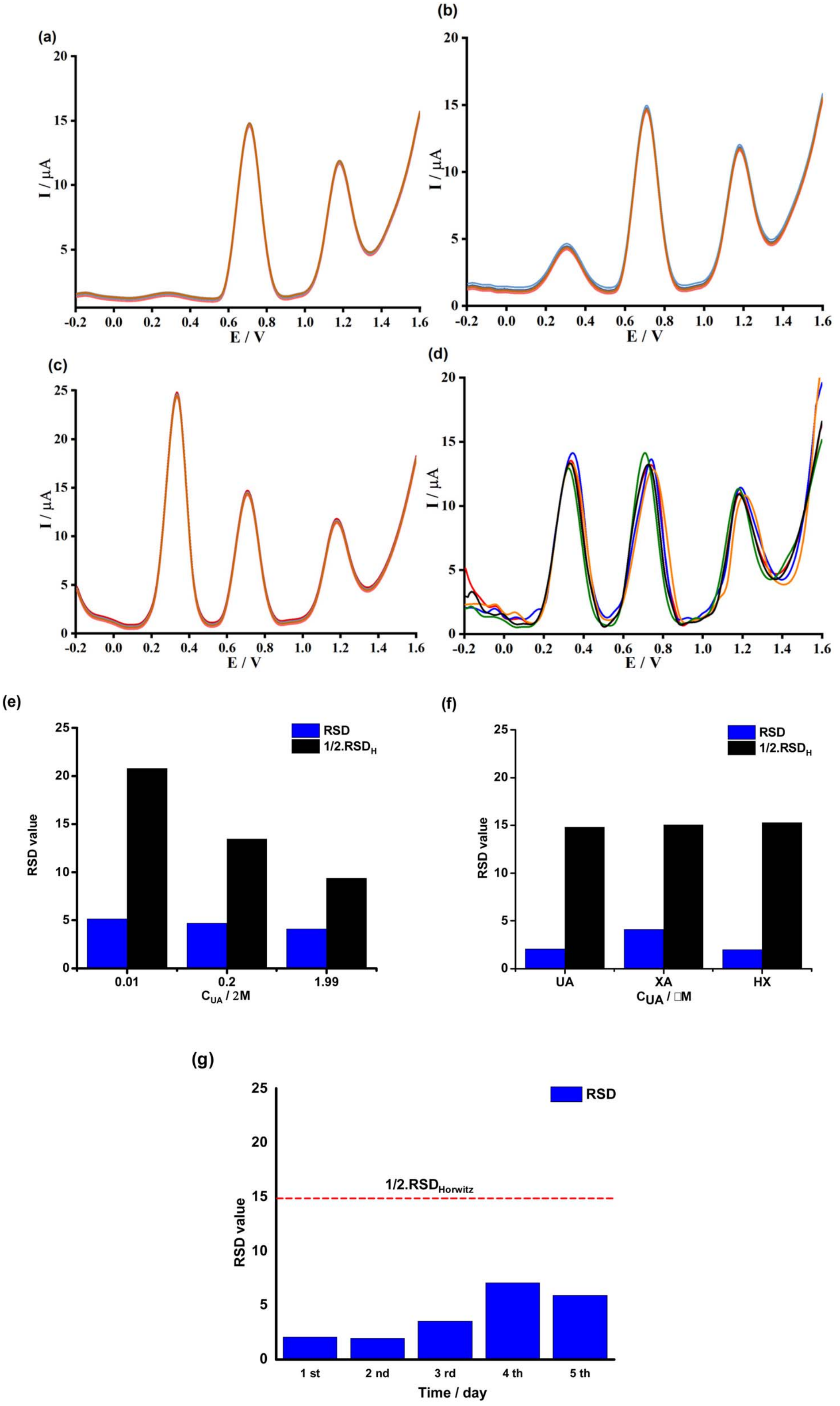

Fig. 10 (a–c) The DPV curves of UA in the co-existence of XA (1.0 µM) and HX (1.0 µM) with nine successive repeated scan tests at orderly C_{UA} (µM): 0.01, 0.20, and 1.99, (d) DPVs of UA at the GCE modified 5 times with Fe_2O_3-RGO in the solution, including 0.1 µM of UA, XA, and HX, (e) statistical evaluation of repeatability: comparison between the experimental (RSD_{exp}) and the theoretical Horwitz limit ($\frac{1}{2}$ $RSD_{Horwitz}$) at three distinct concentrations; (f) statistical assessment of inter-electrode reproducibility comparing RSD_{exp} *vs.* $\frac{1}{2}$ $RSD_{Horwitz}$ ($n = 5$); and (g) long-term stability profile illustrating the current retention and corresponding RSD values after a 1-week storage period.

lowest reported in recent literature for multi-analyte detection. The key innovation lies in its ability to selectively detect UA without interference from its metabolic precursors, XA and HX. This unique capability, combined with a sustainable synthesis method, makes our sensor a promising and robust alternative to existing platforms, addressing a critical need for high selectivity and sensitivity in clinical applications.[48]

3.2.6. Repeatability and reproducibility. The stability and precision of the fabricated sensor were evaluated through a series of repeatability and reproducibility tests, with the results being presented in Fig. 10. The repeatability of the DPV response was assessed by conducting nine successive measurements on a single Fe_2O_3-RGO/GCE at three different UA concentrations (0.01 μM, 0.20 μM, and 1.99 μM) in the presence of co-existing XA and HX. As shown in Fig. 10a–c, the DPV curves for each concentration were highly overlapped, indicating a stable and consistent signal. The low relative standard deviation (RSD) values of 5.14%, 4.70%, and 4.08% for the respective UA concentrations demonstrate the excellent repeatability of the sensor. These values were found to be significantly lower than $\frac{1}{2}$ RSD_H values ($RSD_{Horwitz} = 2^{1-0.5\log C}$, where C is the fraction concentration of the analysis compound) of 20.79%, 13.42%, and 9.35%, confirming the method's high precision and reliability.[57,58]

The reproducibility of the electrode fabrication process was also investigated. This was performed by preparing five separate Fe_2O_3-RGO/GCEs and recording the DPV signals of a solution containing 1.0 μM of UA, XA, and HX with each electrode. As depicted in Fig. 10d, the DPV curves from the different electrodes show a high degree of overlap, with the peak currents for UA being remarkably consistent. The low RSD of 2.07% for the UA peak current, as calculated across the five different electrodes, provides strong evidence for the excellent reproducibility of the fabrication method.[58]

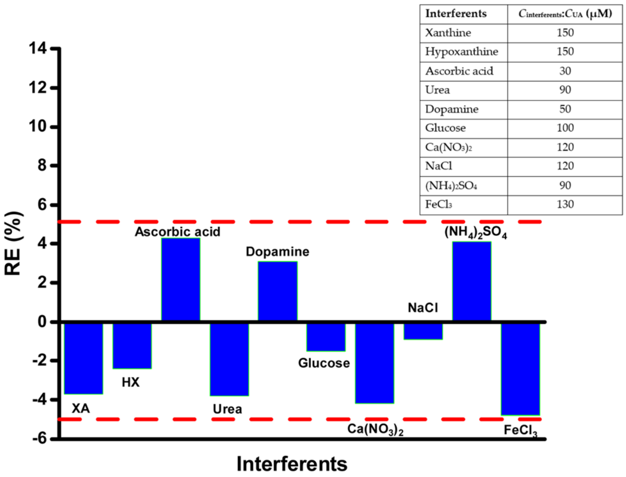

Interferents	$C_{interferents}$:C_{UA} (μM)
Xanthine	150
Hypoxanthine	150
Ascorbic acid	30
Urea	90
Dopamine	50
Glucose	100
$Ca(NO_3)_2$	120
NaCl	120
$(NH_4)_2SO_4$	90
$FeCl_3$	130

Fig. 11 Selectivity profile of the Fe_2O_3-RGO/GCE sensor: bar chart displaying the relative error (RE%) in the DPV response of uric acid (20 μM) in the presence of various potentially interfering species. The red dashed lines indicate the acceptable tolerance limit of ±5%. Inset: table detailing the specific molar concentration ratios ($C_{interferents}$: C_{UA}) used for each interfering species in the selectivity test.

In summary, the satisfactory results obtained from both the repeatability and reproducibility tests confirm the robustness and consistency of the Fe_2O_3-RGO/GCE. The ability of the sensor to produce reliable and consistent signals over multiple consecutive scans and across different independently fabricated electrodes is crucial for its practical application in the routine analysis of UA, XA, and HX in complex samples.

3.2.7. Interferents. The selectivity of the fabricated sensor was rigorously evaluated to ensure its reliable performance in the presence of various potentially interfering species, a crucial step for the intended application in biological matrices. The results are presented in Fig. 11, where the influence of each interferent on the UA signal was quantified using the relative error (RE%) at specified molar ratios.[44,45] A key finding of this investigation was the negligible interference from both XA and HX, which are structurally similar purine metabolites often co-existing with UA. Although isolated albumin was not tested, the subsequent analysis of real urine samples, which naturally contain proteins, demonstrated high recovery rates, suggesting that the sensor surface is robust against significant protein fouling. It was observed that these compounds, even at a molar ratio of 150 times that of UA, resulted in low RE (%) values of only −3.7% and −2.4%, respectively. This outcome is highly significant, as the ability to selectively and accurately determine UA without signal cross-talk from its metabolic precursors addresses a long-standing challenge in electrochemical analysis.

The robustness of the sensor was further validated by assessing the impact of other common interferents typically found in biological and environmental samples. Ascorbic acid, a powerful reducing agent, and dopamine, a neurochemical, both introduced minimal interference, with RE (%) values of 4.3% and 3.1%, respectively. Similarly, other common ions and organic species, such as urea, glucose, $Ca(NO_3)_2$, NaCl, $(NH_4)_2SO_4$, and $FeCl_3$, were shown to have a minimal effect on the UA signal. Even at high molar ratios, the RE (%) values for these species consistently fell within the acceptable range of ±5%,[44,45] with the highest observed interference being −4.8% for $FeCl_3$. These results collectively demonstrate that the fabricated electrode exhibits exceptional selectivity and stability, confirming its suitability for the direct analysis of UA in complex matrices, such as human urine, without the need for extensive sample preparation or separation techniques.

3.2.8. Real samples. To evaluate the practical applicability of the proposed method, urine samples were analyzed using the fabricated Fe_2O_3-RGO/GCE and validated against a well-established reference technique, high-performance liquid chromatography (HPLC). The detailed results of this experiment are presented in Table 3. Initially, the unspiked urine samples were tested, and no UA signal was detected, confirming the absence of the analyte in the original matrix. The samples were then spiked with a known UA concentration of 20 μM and subsequently analyzed by both methods. The DPV method achieved recovery rates ranging from 96% to 104%. These values fall within the acceptable range for analytical standards, demonstrating that matrix components did not cause significant interference and validating the accuracy and robustness of

Table 3 The detection of UA in five urine samples through the DPV and HPLC method

		DPV method		
Sample	UA added (μM)	Found (μM)	Rev. (%)	HPLC (μM)
Urine #1	0	0	104	—[a]
	20	20.8 ± 0.7[b]		19.8 ± 0.2
Urine #2	0	0	98	—
	20	19.7 ± 0.1		20.3 ± 0.5
Urine #3	0	0	96	—
	20	19.1 ± 0.7		20.7 ± 1.3
Urine #4	0	0	103	—
	20	20.6 ± 0.3		19.4 ± 0.6
Urine #5	0	0	97	—
	20	19.4 ± 1.1		19.5 ± 0.6

[a] —not analysis. [b] —mean ± standard deviation ($n = 3$).

the sensor. To further verify the agreement between the two methods, a paired-sample *t*-test was performed on the found concentrations. To rigorously assess the agreement between the proposed sensor and the standard HPLC method, a Paired Student's *t*-test was applied to the results of the five urine samples ($n = 5$). This statistical method is appropriate for small sample sizes when comparing two analytical techniques on the same set of test materials. At a 95% confidence level ($\alpha = 0.05$, two-tailed), the calculated *t*-value was found to be -0.039 for 4 degrees of freedom, $t(4) = -0.039$, $p(\text{2-tailed}) = 0.971 > 0.05$. Furthermore, the 95% Confidence Interval (CI) for the mean difference was calculated to be [−1.46, 1.42] μM. Since this interval explicitly includes zero, it is statistically concluded that there is no significant systematic difference between the concentrations determined by the Fe_2O_3-RGO/GCE sensor and those obtained by the reference HPLC method.

In conclusion, the successful attainment of high recovery rates and the statistical consistency with the HPLC reference method provide compelling evidence for the accuracy, reliability, and practical utility of the Fe_2O_3-RGO/GCE sensor. This demonstrates that the method can be effectively employed for the analysis of UA in complex biological samples without requiring extensive sample pretreatment.

3.2.9. Potential limitations and future directions. While the Fe_2O_3-RGO sensor demonstrates excellent selectivity and sensitivity, certain limitations are acknowledged. The long-term storage stability of the non-enzymatic surface requires further longitudinal study to assess oxidation drift over weeks. Furthermore, the current setup utilizes a standard three-electrode system; future work will focus on miniaturizing this architecture onto screen-printed electrodes to facilitate integration into portable, point-of-care diagnostic devices. To mitigate potential aging effects, future protocols may investigate vacuum storage or lyophilization of the modified interface to prevent atmospheric oxidation.

Additionally, it is acknowledged that a deeper kinetic characterization, specifically the determination of diffusion coefficients for the individual analytes using chronoamperometry, was not conducted in this study due to limitations of the instrumentation. This investigation is planned for future work to further elucidate the mass transport mechanisms at the composite interface. Furthermore, the integration of this sensing material into microfluidic flow cells is anticipated to enable continuous, real-time monitoring capabilities.

4. Conclusions

In this study, an electrochemical sensor based on a Fe_2O_3-RGO composite was successfully developed for the simultaneous determination of UA, XA, and HX. A major achievement of this work is the successful resolution of the long-standing analytical challenge of distinguishing between the overlapping signals of these purine metabolites. This was accomplished through the strategic combination of a conductive RGO matrix, synthesized *via* an environmentally friendly electrochemical method, and catalytic Fe_2O_3 nanoparticles.

The superiority of this method is reflected in its high performance metrics, including excellent sensitivity and a remarkably low detection limit for UA. In contrast to conventional analytical techniques that require complex and time-consuming sample pretreatment, the proposed sensor enables the direct analysis of UA in real biological matrices. The high accuracy demonstrated through real-sample analysis, combined with the proven selectivity and robustness of the electrode, underscores the significant practical value of this research. These findings not only contribute to the advancement of high-performance electrochemical sensors but also provide a powerful, cost-effective, and reliable tool for clinical diagnostics and biomedical monitoring.

Conflicts of interest

The authors declare no conflict of interest.

Data availability

All data supporting this study are available within the article.

References

1 P. C. Gomes-Junior, E. D. Nascimento, K. K. de Lima Augusto, G. P. Longatto, R. C. Faria, E. Piccin and O. Fatibello-Filho, *Microchem. J.*, 2024, **207**, 111931.
2 Y. Zhang, C. Ji, X. Wang, B. Qiu and H. Chen, *Electrochem. Commun.*, 2025, 108006.
3 M. Sekine, M. Fujiwara, K. Okamoto, K. Ichida, K. Nagata, R. Hille and T. Nishino, *J. Biol. Chem.*, 2024, **300**(8).
4 A. F. G. Cicero, F. Fogacci, V. Di Micoli, C. Angeloni, M. Giovannini and C. Borghi, *Int. J. Mol. Sci.*, 2023, **24**, 7027.
5 S. Masrat, V. Nagal, M. Khan, A. Ahmad, M. B. Alshammari, S. Alam, U. T. Nakate, B. Lee, P. Mishra and K. S. Bhat, *ACS Appl. Nano Mater.*, 2023, **6**, 16615–16624.
6 S.-H. Han, K. W. Moon, Y. J. Lee and G.-J. Lee, *Chemosensors*, 2023, **11**, 185.

7 X. Yang, C. He, Y. Qiu, J. Bao, P. Li, Y. Chen, X. Zhou, B. Huang and X. Zheng, *Mater. Chem. Phys.*, 2022, **292**, 126825.

8 S. Arora and N. Verma, *ChemistrySelect*, 2026, **11**, e02016.

9 L. Chelmea, M. Badea, I. Scarneciu, M. A. Moga, L. Dima, P. Restani, C. Murdaca, D. Ciurescu and L. E. Gaman, *Chemosensors*, 2023, **11**, 341.

10 S. Arora, J. Liang, S. K. Fullerton-Shirey and J. E. Laaser, *ACS Mater. Lett.*, 2020, **2**, 331–335.

11 T. Yao, Y. Taniguchi, T. Wasa and S. Musha, *Bull. Chem. Soc. Jpn.*, 1978, **51**, 2937–2941.

12 S. Arora and N. Verma, *RSC Appl. Polym.*, 2024, **2**, 317–355.

13 F. Zhang, Z. Wang, Y. Zhang, Z. Zheng, C. Wang, Y. Du and W. Ye, *Talanta*, 2012, **93**, 320–325.

14 N. T. V. Hoan, N. N. Minh, T. T. K. Nhi, N. Van Thang, V. A. Tuan, V. T. Nguyen, N. M. Thanh, N. Van Hung and D. Q. Khieu, *J. Nanomater.*, 2022, **6**(6), DOI: 10.1155/2020/4350125.

15 N. Le My Linh, D. T. T. Nhan, D. Q. Huong, D. M. Nguyen, N. T. T. Uyen, D. M. Dung, T. N. Dat, L. Van Thanh Son, T. T. T. Toan and D. Q. Khieu, *J. Nanoparticle Res.*, 2024, **26**, 1–16.

16 J. Liang, K. Xu, S. Arora, J. E. Laaser and S. K. Fullerton-Shirey, *Materials*, 2020, **13**, 1089.

17 S. Arora, J. Rozon and J. E. Laaser, *Macromolecules*, 2021, **54**, 6466–6476.

18 R. Pandiyan, P. Rameshkumar and S.-M. Chen, *Process Saf. Environ. Prot.*, 2025, 107446.

19 R. Pandiyan, P. Veerakumar, S.-M. Chen and P. Rameshkumar, *ACS Appl. Nano Mater.*, 2024, **7**, 12507–12520.

20 A. Zhou, J. Bai, W. Hong and H. Bai, *Carbon N. Y.*, 2022, **191**, 301–332.

21 C. A. Ramirez, A. R. Thiruppathi, O. Ozoemena and A. Chen, *Can. J. Chem.*, 2024, **102**, 667–681.

22 S. Jarić, S. Schobesberger, L. Velicki, A. Milovančev, S. Nikolić, P. Ertl, I. Bobrinetskiy and N. Ž. Knežević, *Talanta*, 2024, **274**, 126079.

23 N. Lavanya, C. Sekar, R. Murugan and G. Ravi, *Mater. Sci. Eng., C*, 2016, **65**, 278–286.

24 G. Keles, E. Sifa Ataman, S. B. Taskin, İ. Polatoglu and S. Kurbanoglu, *Biosensors*, 2024, **14**, 238.

25 C. L. Fritsch P, *Int. J. Radiat. Biol.*, 1999, **75**, 1459–1471.

26 G. Geipel, *Coord. Chem. Rev.*, 2006, **250**, 844–854.

27 X. Qiao, R. Bian, S. Li, J. Zhu, F. Wang and C. Liu, *J. Mater. Res.*, 2024, **39**, 2629–2639.

28 J. Liu, J. Li, Y. Chen, X. Tan and C. Yang, *Diamond Relat. Mater.*, 2025, 112413.

29 Z. Huo, S. Arora, V. A. Kong, B. J. Myrga, A. Statt and J. E. Laaser, *Macromolecules*, 2023, **56**, 1845–1854.

30 V. N. Hoang, D. T. N. Hoa, N. Q. Man, L. V. T. Son, L. V. T. Son, V. T. Nguyen, L. T. H. Phong, L. H. Diem, K. C. Ly and H. S. Thang, *Beilstein J. Nanotechnol.*, 2024, **15**, 719–732.

31 S. Y. Toh, K. S. Loh, S. K. Kamarudin and W. R. W. Daud, *Chem. Eng. J.*, 2014, **251**, 422–434.

32 F. Zhang, H. Yang, X. Xie, L. Li, L. Zhang, J. Yu, H. Zhao and B. Liu, *Sens. Actuators, B*, 2009, **141**, 381–389.

33 L. Chen, D. Liu and P. Yang, *RSC Adv.*, 2019, **9**, 12793–12800.

34 G. E. Lloyd, *Mineral. Mag.*, 1987, **51**, 3–19.

35 J. I. Goldstein, D. E. Newbury, J. R. Michael, N. W. M. Ritchie, J. H. J. Scott and D. C. Joy, in *Scanning Electron Microscopy and X-Ray Microanalysis*, Springer, 2017, pp. 15–28.

36 A. Ashraf, R. Wahab, A. A. Al-Khedhairy, A. Khan and F. Rahman, *Mater. Chem. Phys.*, 2024, **316**, 129111.

37 Z. Abasali Karaj Abad, A. Nemati, A. Malek Khachatourian and M. Golmohammad, *J. Mater. Sci. Mater. Electron.*, 2020, **31**, 14998–15005.

38 C. Wu, H. Zhang, Y.-X. Wu, Q.-C. Zhuang, L.-L. Tian and X.-X. Zhang, *Electrochim. Acta*, 2014, **134**, 18–27.

39 D. A. C. Brownson and C. E. Banks, *The Handbook of Graphene Electrochemistry*, 2014.

40 R. T. Kachoosangi, G. G. Wildgoose and R. G. Compton, *Anal. Chim. Acta*, 2008, **618**, 54–60.

41 J. Soleymani, M. Hasanzadeh, N. Shadjou, M. K. Jafari, J. V. Gharamaleki, M. Yadollahi and A. Jouyban, *Mater. Sci. Eng., C*, 2016, **61**, 638–650.

42 E. Laviron, *Electroanalysis*, 1979, **101**, 19–28.

43 C. Li, *Colloids Surf., B*, 2007, **55**, 77–83.

44 F. Xie, X. Lin, X. Wu and Z. Xie, *Talanta*, 2008, **74**, 836–843.

45 H. Zhang, X. Bo and L. Guo, *Sens. Actuators, B*, 2015, **220**, 919–926.

46 B. Rezaei and S. Damiri, *Sens. Actuators, B*, 2008, **134**, 324–331.

47 A. Purwidyantri, C.-H. Chen, L.-Y. Chen, C.-C. Chen, J.-D. Luo, C.-C. Chiou, Y.-C. Tian, C.-Y. Lin, C.-M. Yang, H.-C. Lai and C.-S. Lai, *J. Electrochem. Soc.*, 2017, **164**, B205–B211.

48 N. Verma and S. Arora, *Pharmaceutics*, 2025, **17**, 990.

49 F. Muhammad, G. Dik, S. Kolak, K. K. Gedik, B. Bakar, A. Ulu and B. Ateş, *Electrochim. Acta*, 2023, **439**, 141675.

50 F. Wang, D. Zhao, W. Li, H. Zhang, B. Li, T. Hu and L. Fan, *Microchem. J.*, 2023, **185**, 108154.

51 T. Tang, M. Zhou, J. Lv, H. Cheng, H. Wang, D. Qin, G. Hu and X. Liu, *Colloids Surf., B*, 2022, **216**, 112538.

52 A. U. Rehman, M. Anwar, A. Khan, K. A. Kalhoro, C. Zhang, Y. Zhang, M. Shokouhimehr and Z. Liu, *Microchem. J.*, 2025, **209**, 112821.

53 J. Nong, N. Zhang, A. Wen and C. Hu, *J. Electroanal. Chem.*, 2024, **952**, 117982.

54 L. Liv, *Microchem. J.*, 2023, **195**, 109425.

55 M.-Q. Wang, C. Ye, S.-J. Bao, Y. Zhang, Y.-N. Yu and M. Xu, *Analyst*, 2016, **141**, 1279–1285.

56 P. Gai, H. Zhang, Y. Zhang, W. Liu, G. Zhu, X. Zhang and J. Chen, *J. Mater. Chem. B*, 2013, **1**, 2742–2749.

57 P. R. Dalmasso, M. L. Pedano and G. A. Rivas, 2012, DOI: DOI: 10.1016/j.snb.2012.07.087.

58 I. Taverniers, M. De Loose and E. Van Bockstaele, *TrAC Trends Anal. Chem.*, 2004, **23**, 535–552.